# Article

# Evidence for a single-layer van der Waals multiferroic

Qian Song[1,2,9], Connor A. Occhialini[1,9], Emre Ergeçen[1,9], Batyr Ilyas[1,9], Danila Amoroso[3,4], Paolo Barone[5], Jesse Kapeghian[6], Kenji Watanabe[7], Takashi Taniguchi[8], Antia S. Botana[6], Silvia Picozzi[3], Nuh Gedik[1] & Riccardo Comin[1✉]

Multiferroic materials have attracted wide interest because of their exceptional static[1–3] and dynamical[4–6] magnetoelectric properties. In particular, type-II multiferroics exhibit an inversion-symmetry-breaking magnetic order that directly induces ferroelectric polarization through various mechanisms, such as the spin-current or the inverse Dzyaloshinskii–Moriya effect[3,7]. This intrinsic coupling between the magnetic and dipolar order parameters results in high-strength magnetoelectric effects[3,8]. Two-dimensional materials possessing such intrinsic multiferroic properties have been long sought for to enable the harnessing of magnetoelectric coupling in nanoelectronic devices[1,9,10]. Here we report the discovery of type-II multiferroic order in a single atomic layer of the transition-metal-based van der Waals material $NiI_2$. The multiferroic state of $NiI_2$ is characterized by a proper-screw spin helix with given handedness, which couples to the charge degrees of freedom to produce a chirality-controlled electrical polarization. We use circular dichroic Raman measurements to directly probe the magneto-chiral ground state and its electromagnon modes originating from dynamic magnetoelectric coupling. Combining birefringence and second-harmonic-generation measurements with theoretical modelling and simulations, we detect a highly anisotropic electronic state that simultaneously breaks three-fold rotational and inversion symmetry, and supports polar order. The evolution of the optical signatures as a function of temperature and layer number surprisingly reveals an ordered magnetic polar state that persists down to the ultrathin limit of monolayer $NiI_2$. These observations establish $NiI_2$ and transition metal dihalides as a new platform for studying emergent multiferroic phenomena, chiral magnetic textures and ferroelectricity in the two-dimensional limit.

The recent discovery of intrinsic magnetic order in atomically thin van der Waals (vdW) materials[11,12] has created new opportunities for the study of collective spin phenomena in free-standing two-dimensional (2D) systems and nanoscale devices[13,14]. In past years, substantial efforts have been made to achieve direct electrical control and manipulation of magnetic properties in two dimensions[9,10], but the mechanisms remain unclear. A more promising avenue towards realizing electrical control of 2D magnetism may be found in vdW materials with intrinsic type-II multiferroicity. In type-II multiferroics, the direct coupling between the magnetic and ferroelectric order parameters is enabled by the presence of a spin configuration lacking inversion symmetry[15–17], resulting in a large and robust magnetoelectric response[3,8,18].

Among possible multiferroic vdW materials, several families have been identified[14,19,20], most prominently the transition-metal dihalides ($MH_2$, where M is a transition metal and H is a halogen). Of particular promise is the magnetic semiconductor $NiI_2$ (refs. [19,21–24]), which is host to a rich phase diagram including a type-II multiferroic ground state[2,25,26]. $NiI_2$ crystallizes in the rhombohedral $R\bar{3}m$ structure at room temperature, forming a triangular lattice of $Ni^{2+}$ ions ($3d^8$, $S = 1$) which are stacked along the **c** axis and held together by weak interlayer bonding (Fig. 1a; see also Extended Data Fig. 1 for X-ray and electron diffraction data). The 2D triangular lattice geometrically frustrates the intralayer magnetic exchange interactions that govern the long-range ordering of the local Ni spins[21,22,27]. This leads to a sequence of magnetic phase transitions in $NiI_2$, first to an antiferromagnetic (AFM) state at the Néel temperature $T_{N,1} \simeq 75$ K, and then to a proper-screw helimagnetic ground state below the helimagnetic transition temperature $T_{N,2} \simeq 59.5$ K. The latter exhibits long wavelength helical magnetic structure with propagation vector $\mathbf{Q} = (0.138, 0, 1.457)$ reciprocal lattice units[28] (Fig. 1b). The helimagnetic transition is associated with the

[1]Department of Physics, Massachusetts Institute of Technology, Cambridge, MA, USA. [2]Department of Material Science and Engineering, Massachusetts Institute of Technology, Cambridge, MA, USA. [3] Consiglio Nazionale delle Ricerche CNR-SPIN, c/o Università degli Studi 'G. D'Annunzio', Chieti, Italy. [4]NanoMat/Q-mat/CESAM, Université de Liège, Liège, Belgium. [5]Consiglio Nazionale delle Ricerche CNR-SPIN, Area della Ricerca di Tor Vergata, Rome, Italy. [6]Department of Physics, Arizona State University, Tempe, AZ, USA. [7] Research Center for Functional Materials, National Institute for Materials Science, Tsukuba, Japan. [8] International Center for Materials Nanoarchitectonics, National Institute for Materials Science, Tsukuba, Japan. [9]These authors contributed equally: Qian Song, Connor A. Occhialini, Emre Ergeçen, Batyr Ilyas. ✉e-mail: rcomin@mit.edu
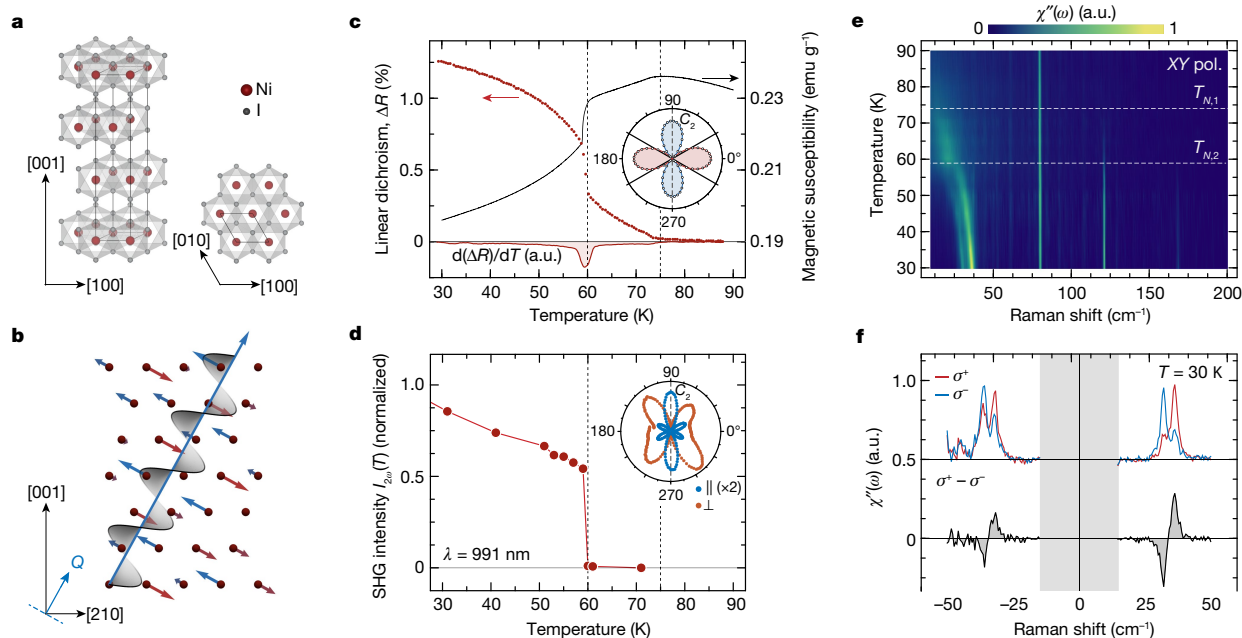
**Fig. 1 | Crystal structure, magnetic order and optical characterization of bulk $NiI_2$. a**, The high-temperature $R\bar{3}m$ structure of $NiI_2$. **b**, The helical magnetic structure of bulk $NiI_2$ below $T_{N,2} = 59.5$ K (see text). **c**, Temperature-dependent linear dichroism ($\Delta R(T)$) measurements on a mono-domain region of bulk $NiI_2$, overlaid on the magnetic susceptibility $\chi_{mag}$. The inset shows the angular dependence of $\Delta R$ at $T = 30$ K; radial lines indicate the crystallographic **a** axes and the dashed line corresponds to the local $C_2$ axis. **d**, Below band gap ($\lambda = 991$ nm) temperature-dependent SHG in bulk $NiI_2$. The inset shows RA-SHG patterns for a monodomain region in the parallel (∥) and perpendicular (⊥) polarization channels with the dashed line corresponding to the $C_2$-axis orientation. Vertical dashed lines in **c** and **d** indicate the $T_{N,1}$ and $T_{N,2}$ transitions. **e**, Temperature-dependent Raman spectra in the $XY$ polarization (pol.) channel. **f**, Circularly polarized Stokes and anti-Stokes Raman spectra of the soft mode excitations for $\sigma^+/\sigma^-$ incident polarization (top) and the net ROA ($\sigma^+ - \sigma^-$) (bottom). a.u., arbitrary units.

appearance of an in-plane electrical polarization perpendicular to the ordering vector[2] and crystal symmetry lowering from rhombohedral to monoclinic[28].

In this study, we investigate the multiferroic states in bulk and few-layer $NiI_2$ crystals[29]. Owing to the complexity of the ground state, which simultaneously breaks mirror, rotational and inversion symmetries, we use a suite of complementary optical techniques to track the multiple signatures of the polar and magneto-chiral orders, as a function of temperature and layer number. Optical birefringence is found to originate from a lowering of the lattice symmetry at both the $T_{N,1}$ and $T_{N,2}$ transitions, and is consistent with a breaking of the **c**-axis three-fold rotational symmetry ($C_{3z}$) and a reduction to a single in-plane two-fold symmetry operation ($C_2$)[30]. We, in addition, use second harmonic generation (SHG) as a probe of inversion symmetry breaking, which, together with lowering of rotational symmetry to $C_2$, enables us to track the presence of polar order down to the single-layer limit. To confirm the presence of magneto-chiral order in the helimagnetic phase of $NiI_2$, we perform Raman spectroscopy with circularly polarized light to resolve a coupled spin-lattice electromagnon excitation with strong optical activity as a signature of spin chirality. These experimental findings are supported by first-principles and Monte Carlo (MC) simulations, altogether providing robust evidence for the persistence of type-II multiferroic order down to single-layer $NiI_2$.

## Optical characterization of bulk $NiI_2$

We first performed high-resolution, single-domain linear dichroism measurements on bulk $NiI_2$—representing the difference in reflectivity $\Delta R$ between two perpendicular, linear polarization states—across the two transitions at $T_{N,1}$ and $T_{N,2}$ (Fig. 1c). The appearance of optical birefringence indicates the breaking of the three-fold ($C_{3z}$) rotational symmetry in the parent $\bar{3}m$ point group, resulting in birefringent domains that are characterized by uniquely oriented, in-plane $C_2$ axes (Extended Data Fig. 2 and Supplemental Information). The temperature dependence of $\Delta R$ bears a marked resemblance to the magnetic susceptibility ($\chi_{mag}$, Fig. 1c), with a kink at $T_{N,1}$ and a sharp jump at $T_{N,2}$. Therefore, the reduction in the lattice rotational symmetry is a direct proxy for the change in the magnetic ground state. We also record the dependence of the linear dichroism signal on the angle of linear incident polarization with respect to the crystallographic axes, $\Delta R(\theta)$. These results (inset of Fig. 1c and Extended Data Fig. 2) display a maximum dichroism of positive sign (blue lobes) for polarization parallel to the crystallographic **a** axis and show the expected two-fold rotational symmetry, confirming that the low-temperature phase is characterized by a local, unique $C_2$ axis.

To confirm the polar nature of the low-temperature symmetry group, we measured SHG in bulk $NiI_2$ from a mono-domain region identified through SHG imaging (Fig. 1d and Extended Data Fig. 3). Electric-dipole SHG (ED-SHG) is used as a direct probe of inversion symmetry breaking[31]. Here, the pure ED-SHG mechanism is ensured by tuning the energy of the fundamental beam to a wavelength $\lambda = 991$ nm that is below the optical bandgap and $d$–$d$ transitions[30]. This is verified with rotational anisotropy SHG (RA-SHG) measurements, which agree well with the ED-SHG tensor elements predicted for the $C_2$ monoclinic point group in the helimagnetic phase (inset of Fig. 1d, Extended Data Fig. 3 and Supplemental Information). For wavelengths in the vicinity of the $d$–$d$ transitions ($\lambda = 780$ and 826 nm), magnetic-dipole SHG originating purely from spin order, which does not necessitate inversion symmetry breaking, is also present (Extended Data Fig. 3 and Supplemental Information). The combined observation of ED-SHG (lattice inversion symmetry breaking) and optical birefringence (rotational symmetry breaking) directly confirms the presence of a polar phase in
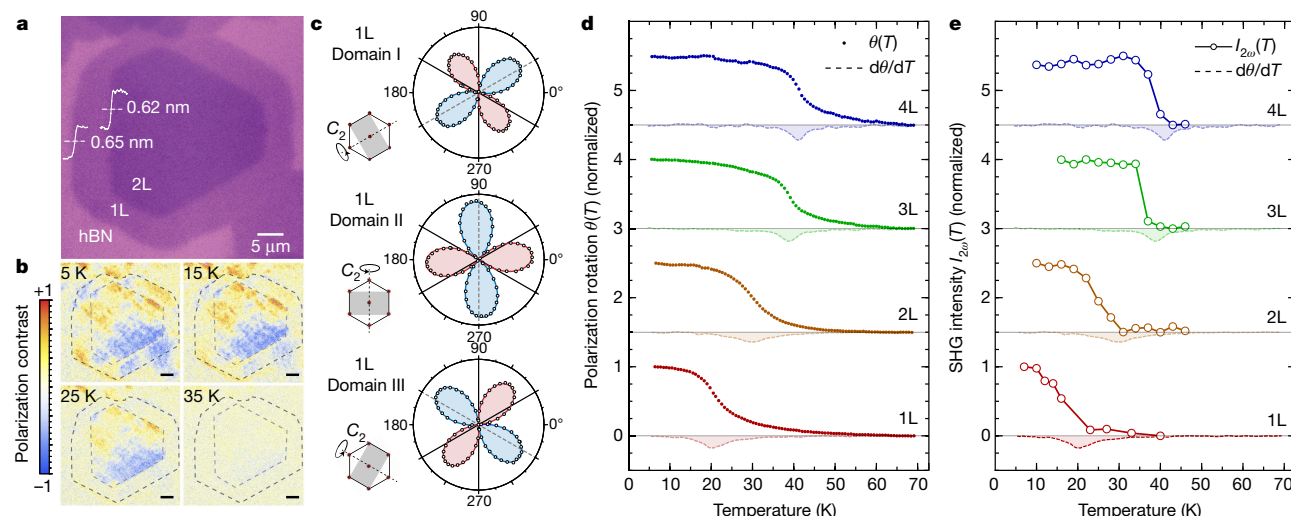
**Fig. 2 | Birefringence and SHG in few- and single-layer NiI$_2$. a**, Optical image of single-layer (1L) and two-layer (2L) NiI$_2$ samples grown on hBN with atomic step height profiles measured by atomic force microscopy (scale bar, 5 μm). **b**, Temperature-dependent polarized microscopy images on the same region in **a**. Dashed lines demarcate the one- and two-layer regions (scale bars, 5 μm). **c**, Angular-dependent linear dichroism $\Delta R(\theta)$ measurements in monolayer NiI$_2$ on three monodomain regions determined from polarized microscopy, as in **b**. Radial lines indicate the crystallographic **a** axes and the dashed lines indicate the orientation of the local $C_2$ axis, as shown in the schematics on the left. **d**, Temperature-dependent, birefringence-induced polarization rotation $\theta(T)$ measurements acquired in monodomain regions of one- to four-layer (4L) NiI$_2$ samples. **e**, Temperature-dependent ED-SHG ($\lambda = 991$ nm) intensity for one- to four-layer samples. Error bars in the SHG data are smaller than the size of the data points. The dashed curves in **d** and **e** represent d$\theta$/d$T$ calculated from layer-dependent $\theta(T)$ data in **d**. Data are normalized to the value at 5 K and offset vertically for clarity.

NiI$_2$ (Supplemental Information) and an underlying single-**Q**, helical magnetic ground state. The resulting electrical polarization induces a bulk photovoltaic effect, which was detected in photocurrent measurements on a thin NiI$_2$ flake (Extended Data Fig. 6).

To underscore the connection between the optical signatures of polar order and the underlying magnetic state, we have performed Raman measurements ($\lambda = 532$ nm) on bulk NiI$_2$. Above $T_{N,1}$, the cross-polarized ($XY$) Raman spectrum of NiI$_2$ shows a single phonon at 80.2 cm$^{-1}$ of $E_g$ symmetry[29]. Our measurements reveal a major change in the Raman response in the magnetically ordered phase, including the appearance of two new high-energy modes around 120.8 and 168.8 cm$^{-1}$ (Fig. 1e), which exhibit polarization selection rules corresponding to single magnon excitations[32,33] (Extended Data Figs. 4 and 5). At low-energy transfer, a broad quasi-elastic signal develops on approaching $T_{N,1}$ (ref. [29]; Fig. 1e). Below $T_{N,2}$, this broad excitation hardens into two sharp and distinct modes (Fig. 1e, f), which have a much more complex set of selection rules compared to the higher energy magnon and phonon excitations (Extended Data Figs. 4 and 5) indicating they are electromagnons[3–7]. In support of this interpretation, circularly polarized excitation reveals a large Raman optical activity (ROA) for the electromagnon peaks (Fig. 1f) that is absent for all other phonon and magnon excitations (Extended Data Fig. 4). The presence of large ROA for the electromagnon highlights it to be a direct signature of magneto-chiral order. The reversal of the ROA between Stokes and anti-Stokes scattering (Fig. 1f) is in agreement with the optical selection rules observed for Raman-active magnetic excitations in previous studies[32].

## Layer-dependent multiferroic order

The baseline optical characterization of bulk samples serves as a blueprint for the exploration of the multiferroic state in few-layer NiI$_2$ samples. Figure 2a shows an optical image of one- and two-layer NiI$_2$ crystals grown by physical vapour deposition on hexagonal boron nitride (hBN). The optical anisotropy of NiI$_2$ is directly captured using cross-polarized microscopy (Methods), signalling the presence of birefringent domains on both the one- and two-layer regions at $T = 5$ K (Fig. 2b). As temperature is increased, the birefringent domains vanish from the single-layer region between $T = 15$ and 25 K, and from the two-layer region between $T = 25$ and 35 K (Fig. 2b). Crucially, a reduction of rotational symmetry from three-fold to two-fold is also observed in single-layer samples, as confirmed by angular-dependent linear dichroism ($\Delta R(\theta)$) measurements (Fig. 2c). Linear dichroism data collected in different domains, determined from the cross-polarized images, show the presence of unique two-fold ($C_2$) axes (highlighted by dashed lines in Fig. 2c). The detailed layer dependence of the rotational symmetry breaking transition is obtained through birefringence-induced polarization rotation measurements ($\theta(T)$; Methods) in Fig. 2d, which reveals a monotonic evolution of the transition temperatures from one- to four-layer samples. The transition temperatures are defined as the values of maximum slope of the polarization rotation signal (where d$\theta$/d$T$ is minimum), yielding 21 K for single-layer, 30 K for two-layer, 39 K for three-layer and 41 K for four-layer flakes (see Extended Data Fig. 10 for three- and four-layer optical images and additional $\theta(T)$ data for one-, two- and four-layer flakes).

Temperature-dependent ED-SHG ($\lambda = 991$ nm) measurements from four- to single-layer NiI$_2$ samples (Fig. 2e) provide complementary information on the breaking of inversion symmetry down to the single-layer limit. For all samples, the SHG intensity shows a clear drop near the transition temperatures derived from the birefringence data. The SHG signal from single-layer samples is genuine as demonstrated by temperature-dependent SHG imaging of multiple monolayer regions (Extended Data Fig. 8). For these SHG spatial maps, we note a temperature-independent residual SHG contrast from single-layer NiI$_2$ samples, which originates at the NiI$_2$–hBN interface owing to surface inversion symmetry breaking. The breaking of the inversion symmetry demonstrated through SHG and the three-fold rotational symmetry breaking observed in birefringence measurements (Fig. 2b) clearly establish the persistence of a polar ground state in few- and single-layer samples (Supplemental Information). In addition, Raman
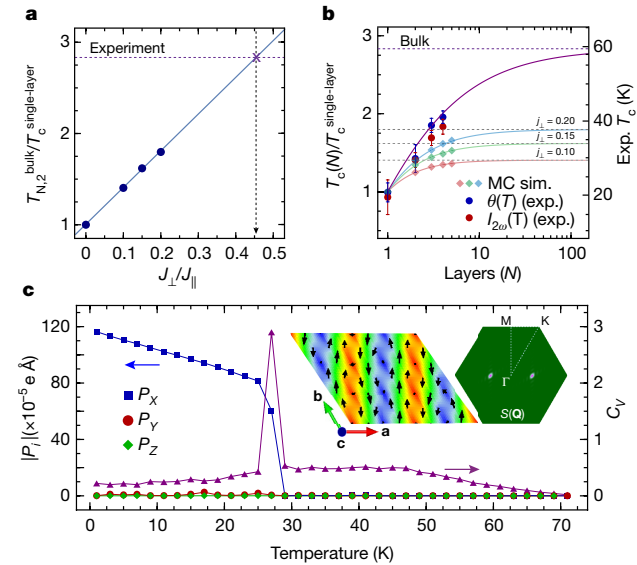
**Fig. 3 | Layer-dependent magnetic transition temperatures and the ground state of single-layer NiI₂. a**, Evolution of the reduced temperature $t$ as a function of the interlayer exchange $J_\perp/J_\parallel$ ($\hat{J}_\perp$), where $t = T_{N,2}^{bulk}/T_c^{single-layer}$ is the ratio of the bulk and single-layer transition temperatures. Circles denote MC estimates and the solid line linearly extrapolates $t$ to larger $J_\perp$. The horizontal dashed line indicates the experimental reduced temperature, $t \simeq 2.8$, whereas the vertical one points to the estimated $J_\perp \simeq 0.45 J_\parallel$. **b**, Evolution of the critical temperature as a function of the number of layers ($N$). Full circles correspond to the experimental (exp.) transition temperatures determined from SHG (red) and birefringence (blue), filled diamonds denote the estimates from MC simulations (sim.) and full lines correspond to the empirical relation provided in the Methods. Dotted horizontal lines represent the bulk transition temperature corresponding to the effective interlayer interaction. **c**, Electrical polarization components $|P_i|$ in units of $10^{-5}$ e Å (absolute value, closed squares) and specific heat ($C_V$, triangles) as a function of temperature, relative to the proper-screw spiral order represented in the insets (for the spin texture, the black arrows represent in-plane components of the spins and the colour map indicates the out-of-plane spin component with red (blue) denoting $s_z = +(-)1$, $S(\mathbf{Q})$ represents the spin structure factor, corresponding to the single-$\mathbf{Q}$ helical spin configuration $\mathbf{Q}$), as obtained by MC simulations.

measurements reveal the persistence of the magnetic soft modes down to the two-layer limit (Extended Data Fig. 9). The quantitative agreement of the transition temperatures from these independent measurements and the smooth trend of these optical signatures as the layer number is reduced from the bulk to the monolayer therefore offer strong evidence for the survival of the polar helimagnetic phase down to the monolayer limit in NiI₂.

## Theoretical modelling

The observed reduction of the transition temperature as the layer number is decreased is strongly indicative of the relevant role played by the interlayer exchange interaction, as also reported for other 2D magnets[12,33–37], and the finite transition temperature detected in the monolayer sample points to a non-negligible magnetic anisotropy.

We performed MC simulations to investigate further the effect of the interlayer exchange interaction on the helimagnetic transition temperature $T_c$. Our starting model is the classical 2D anisotropic Heisenberg model recently introduced for a NiI₂ monolayer[22], supplemented by a nearest-neighbour AFM interlayer exchange $J_\perp$ in order to describe the bulk phase. The presence of anisotropic interactions

guarantees a finite-temperature transition to a long-range ordered magnetic phase even in the monolayer (Fig. 3c). In addition, the transition temperature of the bulk system is found to increase proportionally with $J_\perp$ (Fig. 3a). Experimentally, the helimagnetic transition temperature of the single-layer sample is strongly reduced from its bulk value, being $T_{N,2}/T_c^{single-layer} \simeq 2.8$. A linear extrapolation of the MC estimates for transition temperatures as a function of $J_\perp$ enables the estimation of a large interlayer exchange, $J_\perp \simeq 0.45 J_\parallel$, where $J_\parallel$ is the dominant ferromagnetic (FM) intralayer interaction. Using $J_\parallel \simeq 7$ meV (ref. [22]), the estimated interlayer exchange is $J_\perp = 3.15$ meV; this is in good agreement with the value we directly calculated by means of density functional theory (DFT) calculations for two-layer NiI₂, that is, $J_\perp^{(DFT)} \simeq 3$ meV. The evolution of transition temperatures as a function of the sample thickness has also been estimated with MC simulations for a different number $N$ of layers ($N$ ranging from 1 to 5) and at fixed $J_\perp$. Notably, all MC estimates as well as the experimental data are well described by a simple empirical formula that depends only on the ratio of bulk and single-layer transition temperatures, with no fitting parameters, as shown in Fig. 3b.

The possible onset of a magnetically induced electric polarization in single-layer NiI₂ was investigated further in the framework of the generalized spin-current (or Katsura–Nagaosa–Balatsky (gKNB)) model[38], in which an electric dipole may be induced by spin pairs according to the general expression $\mathbf{P}_{ij} = M \cdot \mathbf{S}_i \times \mathbf{S}_j$, where $\mathbf{P}$, $M$ and $\mathbf{S}$ represent the electric polarization, coupling tensor and spin, respectively, while $i$ and $j$ denote the Ni sites in plane. The 3×3 $M$ tensor was evaluated from first principles, and then used to estimate the polarization of the NiI₂ monolayer from MC simulations. As shown in Fig. 3c, a proper-screw spiral propagating along the **a** lattice vector stabilizes below $T_c \lesssim 27$ K, which is in reasonable agreement with the experimental value of 21 K. The corresponding magnetic point group is the polar 21' group, with the two-fold rotational axis and the electric polarization coinciding with the spiral propagation vector and hence with the **a** axis, in agreement with the optical measurements. Within the gKNB model, the handedness of the spin spiral uniquely determines whether the electric polarization is parallel or antiparallel to the polar axis. Furthermore, we notice that when the magnetic helix is slanted from the basal plane with a propagation vector $\mathbf{Q} = (0.138, 0, 1.457)$, as occurs in bulk samples, the purely spin-induced polarization as evaluated from our estimated $M$ tensor is always parallel to the crystallographic **a** axis.

## Discussion

NiI₂, down to the 2D limit, is an example of improper electronic ferroelectricity, in which the electric polarization is driven by the emergence of an inversion-symmetry-breaking magnetic order (such as the proper-screw spin helix) in an otherwise centrosymmetric lattice. The propensity for such spin-spiral ordering in the single-layer limit can be associated with the significant frustration of the intralayer exchange interactions on the underlying triangular lattice, along with crucial magnetic anisotropy effects[22]. Furthermore, NiI₂ shows superexchange mediated by the extended 5p states of the iodine ligands, the latter also introducing a significant spin–orbit coupling (SOC). As a result, non-negligible spin interactions beyond nearest-neighbour Ni sites play a relevant role in the stabilization of the resulting proper-screw spin helix, the latter giving rise to SOC-induced electric polarization, as described by the gKNB model[38]. In this framework, the observation of SHG and birefringence in monolayer NiI₂ is consistent with the proposed theoretical picture, providing a direct indication of a non-centrosymmetric polar magnetic texture that develops below the identified Curie temperature of 21 K. The observed suppression of the multiferroic transition temperature with reducing layer number further enabled us to clarify the role of the interlayer exchange interactions, which are known to contribute to the orientation of the spin-rotation plane and magnetic ordering vector in the bulk[27,28].

Our results point to the crucial role of SOC and the orbital extension of the ligands in modulating both magnetic anisotropies and exchange interactions beyond nearest-neighbour , ultimately determining the magnetic ground state among closely lying, competing phases[22,49]. This indicates that changing the ligand could be a powerful tuning method to realize new exotic magnetic ground states in two dimensions, including helices, cycloids and skyrmions with unique topological and multiferroic properties[21,22,39]. In addition, our observations of a complex magnetic ground state in an atomically thin vdW crystal introduces new avenues for exploring multiferroicity that are inherently unique to 2D systems. These include the robust and direct electrical control of magnetism through electrostatic doping or external fields and currents, or the realization of new interfacial multiferroic properties in artificial vdW heterostructures. Moreover, 2D materials with gate-tuneable magnetoelectric coupling might offer a new platform for continuous tuning of multiferroic systems towards quantum critical behaviour[40]. Although our optical measurements establish the persistence of multiferroicity in $NiI_2$ to the monolayer limit, further characterization through piezo-response force microscopy or high-sensitivity pyroelectric current measurements will be important in the exploration of ferroelectric order in greater detail and to assess its potential for future device applications.

## Conclusion

In conclusion, our results represent the observation of an intrinsic multiferroic phase in the single-layer limit. Multiple complementary optical signatures confirm the persistence of ferroelectricity and inversion-symmetry-breaking magnetic order down to monolayer $NiI_2$ with a transition temperature of $T = 21$ K. These results introduce the physics of type-II multiferroics into the area of vdW materials. These findings create new opportunities for studying and optimizing the interplay of magnetic and dielectric properties in next-generation nanoscale devices.

## Online content

Any methods, additional references, Nature Research reporting summaries, source data, extended data, supplementary information, acknowledgements, peer review information; details of author contributions and competing interests; and statements of data and code availability are available at https://doi.org/10.1038/s41586-021-04337-x.

1. Matsukura, F., Tokura, Y. & Ohno, H. Control of magnetism by electric fields. *Nat. Nanotechnol.* **10**, 209–220 (2015).
2. Kurumaji, T. et al. Magnetoelectric responses induced by domain rearrangement and spin structural change in triangular-lattice helimagnets $NiI_2$ and $CoI_2$. *Phys. Rev. B* **87**, 014429 (2013).
3. Tokura, Y., Seki, S. & Nagaosa, N. Multiferroics of spin origin. *Rep. Prog. Phys.* **77**, 076501 (2014).
4. Pimenov, A. et al. Possible evidence for electromagnons in multiferroic manganites. *Nat. Phys.* **2**, 97–100 (2006).
5. Rovillain, P. et al. Magnetoelectric excitations in multiferroic $TbMnO_3$ by Raman scattering. *Phys. Rev. B* **81**, 054428 (2010).
6. Kibayashi, S., Takahashi, Y., Seki, S. & Tokura, Y. Magnetochiral dichroism resonant with electromagnons in a helimagnet. *Nat. Commun.* **5**, 4583 (2014).
7. Khomskii, D. Classifying multiferroics: mechanisms and effects. *Physics* **2**, 20 (2009).
8. Spaldin, N. A. & Ramesh, R. Advances in magnetoelectric multiferroics. *Nat. Mater.* **18**, 203–212 (2019).
9. Huang, B. et al. Electrical control of 2D magnetism in bilayer $CrI_3$. *Nat. Nanotechnol.* **13**, 544–548 (2018).
10. Jiang, S., Li, L., Wang, Z., Mak, K. F. & Shan, J. Controlling magnetism in 2D $CrI_3$ by electrostatic doping. *Nat. Nanotechnol.* **13**, 549–553 (2018).
11. Gong, C. et al. Discovery of intrinsic ferromagnetism in two-dimensional van der Waals crystals. *Nature* **546**, 265–269 (2017).
12. Huang, B. et al. Layer-dependent ferromagnetism in a van der Waals crystal down to the monolayer limit. *Nature* **546**, 270–273 (2017).
13. Burch, K. S., Mandrus, D. & Park, J. G. Magnetism in two-dimensional van der Waals materials. *Nature* **563**, 47–52 (2018).
14. Mak, K. F., Shan, J. & Ralph, D. C. Probing and controlling magnetic states in 2D layered magnetic materials. *Nat. Rev. Phys.* **1**, 646–661 (2019).
15. Astrov, D. N. The magnetoelectric effect in antiferromagnetics. *Sov. Phys. – JETP* **11**, 708 (1960).
16. Rado, G. T. & Folen, V. J. Observation of the magnetically induced magnetoelectric effect and evidence for antiferromagnetic domains. *Phys. Rev. Lett.* **7**, 310–311 (1961).
17. Newnham, R. E., Kramer, J. J., Schulze, W. A. & Cross, L. E. Magnetoferroelectricity in $Cr_2BeO_4$. *J. Appl. Phys.* **49**, 6088–6091 (1978).
18. Kimura, T. et al. Magnetic control of ferroelectric polarization. *Nature* **426**, 55–58 (2003).
19. McGuire, M. A. Crystal and magnetic structures in layered, transition metal trihalides and trihalides. *Crystals* **7**, 121 (2017).
20. Lai, Y. et al. Two-dimensional ferromagnetism and driven ferroelectricity in van der Waals $CuCrP_2S_6$. *Nanoscale* **11**, 5163–5170 (2019).
21. Botana, A. S & Norman, M. R. Electronic structure and magnetism of transition metal dihalides: bulk to monolayer. *Phys. Rev. Mater.* **3**, 44001 (2019).
22. Amoroso, D., Barone, P. & Picozzi, S. Spontaneous skyrmionic lattice from anisotropic symmetric exchange in a Ni-halide monolayer. *Nat. Commun.* **11**, 5784 (2020).
23. Pollini, I., Thomas, J. & Lenselink, A. Optical properties of layered transition-metal iodides. *Phys. Rev. B* **30**, 2140–2148 (1984).
24. Ju, H. et al. Possible persistence of multiferroic order down to bilayer limit of van der Waals material $NiI_2$. *Nano Lett.* **21**, 5126–5132 (2021).
25. Kurumaji, T. Spiral spin structures and skyrmions in multiferroics. *Phys. Sci. Rev.* https://doi.org/10.1515/psr-2019-0016 (2020).
26. Amoroso, D., Barone, P. & Picozzi, S. Interplay between single-ion and two-ion anisotropies in frustrated 2D semiconductors and tuning of magnetic structures topology. *Nanomaterials* **11**, 1873 (2021).
27. Friedt, J. M., Sanchez, J. P. & Shenoy, G. K. Electronic and magnetic properties of metal diiodides $MI_2$ (M = V, Cr, Mn, Fe, Co, Ni, and Cd) from $^{129}I$ Mössbauer spectroscopy. *J. Chem. Phys.* **65**, 5093–5102 (1976).
28. Kuindersma, S., Sanchez, J. & Haas, C. Magnetic and structural investigations on $NiI_2$ and $CoI_2$. *Phys. B+C* **111**, 231–248 (1981).
29. Liu, H. et al. Vapor deposition of magnetic van der Waals $NiI_2$ crystals. *ACS Nano* **14**, 10544–10551 (2020).
30. Kumdersma, S. R., Boudewijn, P. R. & Haas, C. Near infrared d-d transitions of $NiI2$, $CdI2:Ni2+$, and $CoI_2$. *Phys. Stat. Sol. (b)* **108**, 187–194 (1981).
31. Xiao, J. et al. Intrinsic two-dimensional ferroelectricity with dipole locking. *Phys. Rev. Lett.* **120**, 227601 (2018).
32. Cenker, J. et al. Direct observation of two-dimensional magnons in atomically thin $CrI_3$. *Nat. Phys.* **17**, 20–25 (2021).
33. Jin, W. et al. Raman fingerprint of two terahertz spin wave branches in a two-dimensional honeycomb Ising ferromagnet. *Nat. Commun.* **9**, 5122 (2018).
34. Deng, Y. et al. Gate-tunable room-temperature ferromagnetism in two-dimensional $Fe_3GeTe_2$. *Nature* **563**, 94–99 (2018).
35. Sivadas, N., Okamoto, S., Xu, X., Fennie, C. J. & Xiao, D. Stacking-dependent magnetism in bilayer $CrI_3$. *Nano Lett.* **18**, 7658–7664 (2018).
36. Akram, M. et al. Moiré skyrmions and chiral magnetic phases in twisted $CrX_3$ (X = I, Br, and Cl) bilayers. *Nano Lett.* **21**, 6633–6639 (2021).
37. Nguyen, T. P. T., Yamauchi, K., Oguchi, T., Amoroso, D. & Picozzi, S. Electric-field tuning of the magnetic properties of bilayer $VI_3$: a first-principles study. *Phys. Rev. B* **104**, 014414 (2021).
38. Xiang, H. J., Kan, E. J., Zhang, Y., Whangbo, M.-H. & Gong, X. G. General theory for the ferroelectric polarization induced by spin-spiral order. *Phys. Rev. Lett.* **107**, 157202 (2011).
39. Prayitno, T. B. Controlling phase transition in monolayer metal diiodides $XI_2$ (X: Fe, Co, and Ni) by carrier doping. *J. Phys. Condens. Matter* **33**, 335803 (2021).
40. Narayan, A., Cano, A., Balatsky, A. V. & Spaldin, N. A. Multiferroic quantum criticality. *Nat. Mater.* **18**, 223–228 (2019).

# Article

## Methods

### Growth and characterization of few-layer NiI₂ crystals

Bulk-like NiI₂ crystals were grown on 300 nm SiO₂/Si and few-layer crystals were grown on hBN substrates by physical vapour deposition (PVD) in a horizontal single-zone furnace equipped with a 0.5 inch diameter quartz tube at ambient pressure. hBN was mechanically exfoliated and transferred onto 300 nm SiO₂/Si substrates and then annealed in vacuum at 700 °C for 1 h before the growth. In a typical synthesis, 0.1 g of NiI₂ powder (99.5%, anhydrous, Alfa Aesar) was positioned at the centre of the furnace as the source material and the SiO₂/Si substrate was placed downstream at the maximum temperature gradient point. The furnace was purged by pumping the quartz tube below 0.1 Torr and then refilled with 99.99% Ar gas three times. When growing bulk-like NiI₂ crystals, the furnace was heated to 450 °C in 15 min and held at that temperature for 10 min. For few-layer NiI₂ samples, the furnace was heated to 380–420 °C in 15 min and then the SiO₂/Si substrate was taken out immediately and stored inside a nitrogen-filled glove box (O₂, <0.5 ppm; H₂O, <0.5 ppm). The sample thickness was determined by atomic force microscopy (AFMWorkshop HR), which was performed inside a separate nitrogen-filled glovebox (O₂, <100 ppm; H₂O, <1 ppm), using a silicon probe in tapping mode. The electron diffraction (JEOL HRTEM) was performed on a 7 nm thick PVD-grown NiI₂ flake using a transmission electron microscope. The flake was picked up and dropped down using the dry transfer technique onto a $SiN_x$ membrane with 2 μm pores (NORCADA)[41].

### Growth and characterization of single-crystal NiI₂

Single-crystal NiI₂ was grown by chemical vapour transport, from elemental precursors with molar ratio Ni:I = 1:2, at a temperature gradient 700 °C to 500 °C. The magnetic susceptibility was measured during field cooling at 0.9 T applied out of plane, using a magnetic property measurement system (MPMS-3, Quantum Design Inc.). X-ray diffraction of chemical vapour transport grown crystals was performed in Bragg geometry using Cu K$\alpha$ radiation (PANalytical), and the refined unit cell at room temperature was $a = 3.91$ Å, $c = 19.93$ Å.

### Device fabrication for bulk photovoltaic effect measurements

The photocurrent device was fabricated by depositing two Ti(5nm)/Au(50 nm) electrodes on a sapphire substrate using a 20 μm wide wire mask. A PVD-grown bulk-like NiI₂ flake was then picked up and dropped down across the gap using a polymer-based dry transfer technique. To minimize the exposure to moisture, the polymer was dissolved in anhydrous chloroform inside the glovebox. To ensure a good and uniform electric contact, a carbon copy of the metal pads was created using the same dry transfer technique and stacked on top of the sample to provide a vertically symmetric contact. We used a 0.3 mW linearly polarized 532 nm laser for the photocurrent measurement. The current was measured using a Keithley 2401 current meter, and the magnetic field was applied perpendicular to the electric field in plane using a 1 T electromagnet from Montana Instruments.

### Raman spectroscopy measurements

Polarized Raman experiments were performed in a back-scattering geometry using a confocal microscope spectrometer (Horiba LabRAM HR Evolution) with a ×50 objective lens and 532 nm laser excitation at a power of 300 and 40 μW for bulk and few-layer samples, respectively. Scattered light was dispersed by a 1,800 lines mm⁻¹ grating and detected with a liquid nitrogen cooled charge-coupled device camera. The spectrometer integration time was 30 and 60 min for bulk and few-layer samples, respectively, and each scan was taken twice and then averaged before analysis. Polarized Raman spectra were recorded with a linearly polarized incident beam. For angle-resolved polarized Raman spectroscopy measurements, an achromatic half-wave plate was placed just before the objective and rotated in steps of 7.5° from 0°

to 180°. An analyser was placed in front of the spectrometer entrance and kept vertical and horizontal for parallel (*XX*) and perpendicular (*XY*) configurations, respectively. For circularly polarized measurements, an achromatic quarter-wave plate was placed in front of the objective with fast axis oriented at +45° and −45° with respect to the incident linear polarization for $\sigma^+$ and $\sigma^-$ circular incident polarization, respectively. For the reported circularly polarized spectra, no analysing polarizer was used. Temperature-dependent measurements in the range of 5–300 K were performed using a Montana Instruments closed-cycle optical cryostat.

### Birefringence measurements

A supercontinuum light source (NKT Photonics, Fianium) monochromatized to $\lambda = 532$ nm and 550 nm, and a bandwidth of approximately 1 nm, was used as excitation for angular-dependent linear dichroism and birefringence-induced polarization rotation measurements, respectively. All measurements were performed at normal incidence in a Montana Instruments closed-cycle optical cryostat. Linear dichroism measurements were performed with a photo-elastic modulator (PEM; PEM-100, Hinds Instruments) on the incident path of the optical setup. The beam incident on the PEM was prepared with linear polarization making an angle of 45° with respect to the PEM fast axis and the amplitude was modulated with a mechanical chopper. The PEM retardance was set to 0.5$\lambda$ to modulate the incident polarization between the +45° and −45° linear polarization states. The light was then focused onto the sample using a ×50 objective lens. The back-scattered light was measured by an amplified photodiode (ThorLabs PDA100A2), in which the output was connected to a lock-in amplifier (Stanford Instruments SR865A) referenced to the second harmonic of the fundamental PEM frequency $f = 50$ kHz. The total reflectance of the sample, used as a normalization, was monitored by a second lock-in amplifier referenced to the chopping frequency $f = 557$ Hz.

To perform angular-dependent linear dichroism measurements, the angle of the perpendicular linear polarization states created by the PEM was varied across the crystal using a zero-order half-wave plate placed just before the objective. To ensure the angular dependence was recorded from a uniform, monodomain region of the sample, polarized microscopy images were first recorded at the base temperature $T = 5$ K. The sample was held at this temperature for the duration of the angular-dependent measurements to maintain the same distribution of birefringent domains. Birefringence-induced polarization rotation measurements on the few- and single-layer samples were performed with the PEM on the detection path of the optical setup with a retardance amplitude of 0.486$\lambda$, using a lock-in amplifier at the second harmonic of the fundamental PEM frequency for signal collection. The unrotated incident beam was kept parallel to the PEM fast axis and analysed by a polarizer at 45°, before being measured by the photodiode. This setup provided a sensitivity down to 10 μrad.

Polarized microscopy was performed with a broadband visible LED light source, a standard complementary metal–oxide–semiconductor-based monochrome camera and Glan–Thompson polarizers on both the input and output light paths in reflection geometry. A detuning of 0.5 and 2.0 degrees from a cross-polarized configuration was used to maximize the contrast from birefringent domains and a 5 and 2 s integration time was used for the images of the few-layer and bulk samples, respectively (Extended Data Fig. 7). Cross-polarized contrast images were obtained as a function of temperature by autocorrelating the images for different temperatures to overlap with a high-temperature ($T > T_{N,1}$) reference, and by subtracting the low- and high-temperature images.

### Layer-dependent SHG microscopy

In SHG microscopy, an objective lens (Olympus LMPlanFL-N ×50) focuses an ultrashort laser beam onto the sample located in a cryostat

(Janis ST-500). For wavelength-dependent SHG experiments, we used an optical parametric amplifier (ORPHEUS, Light Conversion) seeded with a regenerative amplifier (PHAROS SP-10-600-PP, Light Conversion) These enabled us to tune the output wavelength in a wide spectral range. The estimated spot size on the sample was approximately 2 μm. The laser fluence incident on the sample was set to 1 mJ cm⁻². No sample damage or degradation was observed during the measurements. On reflection, the second harmonic component of the beam radiated from the sample was selected by a dichroic mirror and a monochromator with 2 nm spectral resolution. The second harmonic photons were detected and counted using a photomultiplier tube (Hamamatsu PMT) and a dual-channel gated photon counter (Stanford Research SR400). To decrease the background and dark counts, the photon counter was synchronized and gated with laser pulses. To perform SHG imaging (Extended Data Fig. 8), we kept the sample location fixed and rotated a motorized mirror to scan the laser across the sample. The polarization resolved SHG traces are obtained by rotating the incident light polarization with a half-wave plate and selecting the polarization of the second harmonic signal with a wire-grid polarizer (Extended Data Fig. 3).

### Spin model and MC simulations

To describe the magnetic properties of the system, we adopted the 2D anisotropic Heisenberg model derived for a NiI₂ monolayer[22] supplemented by a nearest-neighbour AFM interlayer interaction accounting for the exchange between rhombohedral-stacked layers:

$$H = \frac{1}{2} \sum_{ij} (\mathbf{S}_i^{(e)} \cdot J_{ij} \cdot \mathbf{S}_j^{(e)} + \mathbf{S}_i^{(o)} \cdot J_{ij} \cdot \mathbf{S}_j^{(o)}) + \sum_i \mathbf{S}_i \cdot A_i \cdot \mathbf{S}_i + J_\perp \sum_{<ij>} \mathbf{S}_i^{(e)} \cdot \mathbf{S}_j^{(o)} \quad (1)$$

Here e and o label even and odd layers perpendicular to the **c** axis, respectively, the first sum extends to the third nearest-neighbour within each plane and the last sum is restricted to nearest-neighbours belonging to different layers. We used the interlayer exchange $J_{ij}$ and single-site anisotropy $A_i$ tensors evaluated from first principles for the NiI₂ monolayer[22]; the non-negligible anisotropic terms guarantee a finite-temperature long-range magnetic order, with a triple-**Q** topological phase competing with a single-**Q** spiral configuration. The anisotropic part of the exchange tensor was accordingly rescaled to 60% of the ab initio estimate, thus favouring the spin-spiral solution, in agreement with the breaking of the three-fold rotational symmetry experimentally detected. We set the energy scale as $J_\parallel = -J^{liso}$, where $J^{liso}$ represents the isotropic nearest-neighbour intralayer interaction as defined in[22].

We performed MC simulations using a standard Metropolis algorithm on rhombohedral-stacked triangular lattices (rhombohedral supercells in hexagonal setting) in a slab geometry to simulate multilayer (bulk) NiI₂. We used $10^5$ MC steps for thermalization and $5 \times 10^5$ MC steps for statistical averaging at each simulated temperature. Simulations were performed on $24 \times 24$ lattices in a slab geometry comprising up to five layers of triangular NiI₂ (and up to 2,880 spins) with 2D periodic boundary conditions, and on $8 \times 8 \times 8$ hexagonal supercells (comprising 1,536 spins) with three-dimensional periodic boundary conditions for the bulk rhombohedral system. The transition temperature was identified by the peak in the specific heat of the spin model. All MC results for multilayer slabs at different values of the interlayer exchange $J_\perp$ are well described by a simple empirical function:

$$T_c(N) = T_c^{single-layer} \tanh\left( b \ln N + \frac{1}{2} \ln \frac{t+1}{t-1} \right) \quad (2)$$

where $t = T_{N,2}/T_c^{single-layer}$ is the reduced temperature, $N$ is the number of layers and the coefficient $b = 1.05$ was obtained by fitting only the $J_\perp = 0.1J_\parallel$ data points.

### Generalized spin-current model for magnetically induced polarization

Within the generalized spin-current gKNB model[38], the total polarization is given by

$$\mathbf{P} = \frac{1}{2N} \sum_{ij} M_{ij} \cdot \mathbf{S}_i \times \mathbf{S}_j \quad (3)$$

where $N$ is the number of magnetic sites and we have restricted the sum to intralayer nearest-neighbours. The $M$ tensor was evaluated from first principles for a spin pair parallel to the **a** axis using the four-state method[38] (the tensor of equivalent bonds is readily obtained by enforcing crystalline symmetries). The dominant tensor components found are $M_{22} = 348 \times 10^{-5}$ e Å and $M_{23} = -520 \times 10^{-5}$ e Å, the other components being zero or smaller than approximately $30 \times 10^{-5}$ e Å. Assuming a proper-screw spiral with positive/negative handedness $\tau = \pm 1$ propagating along the **a** ($x$) axis with pitch $2\delta$, the gKNB model predicts $P_x \equiv P_\parallel = 3M_{22}\sin(\tau\delta)/2$, in agreement with numerical MC calculations. For the proper-screw spiral propagating in the **Q** = (0.138,0,1.457) direction, with the spins rotating in a plane making an angle $\theta = 55°$ as observed in bulk NiI₂ (ref. [28]), the electric polarization predicted by the gKNB model lies in the $ab$ plane and is perpendicular to the in-plane projection of **Q**, $P_\perp = \sqrt{3} [M_{22}\cos\theta - 2M_{23}\sin\theta]\sin(0.138\tau)/2$. In both cases, handedness $\tau$ determines the sign of **P**, that is always parallel to the crystallographic axis **a**.

### First-principles calculations

We used DFT to estimate the interlayer exchange interaction and the $M$ tensor of the gKNB model. The interlayer coupling $J_\perp$ was estimated from the energy difference between a FM and AFM stacking of ferromagnetically ordered NiI₂ layers ($\Delta E = E_{FM} - E_{AFM}$). A rhombohedral-stacked bilayer was constructed starting from the optimized NiI₂ monolayer, with lattice parameter $a \simeq 3.96$ Å and an interlayer distance of about 6.54 Å, in agreement with the previously reported bulk value[19]. A vacuum distance of about 18.45 Å was introduced between periodic copies of the free-standing bilayer along the **c** axis. To check the consistency of our results, we performed DFT calculations using both the projector-augmented wave method as implemented in the VASP code[42,43] and the all-electron, full potential code WIEN2k[44], based on the augmented plane wave plus local orbital basis set. Ni 3$p$, 3$d$ and 4$s$ and I 5$s$ and 5$p$ were treated as valence states in VASP calculations, with a plane-wave cut-off of 500 eV and an $18 \times 18 \times 2$ $k$-point mesh for Brillouin-zone integration. In the WIEN2k calculations, a muffin-tin radius of 2.5 Å was used for both Ni and I atoms, and an $RK_{max}$ of 7.0 (i.e., the smallest atomic sphere radius ($R$) and the largest K-vector ($K_{max}$) product). A $k$-mesh of $20 \times 20 \times 2$ was used for the Brillouin-zone sampling. For consistency with previous monolayer calculations[22], we used the Perdew–Burke–Erzenhof (PBE) version of the generalized gradient approximation as the exchange-correlation functional[45] and performed PBE+U calculations[46] within the Liechtenstein approach[47], setting the effective on-site Coulomb and exchange parameters on the localized Ni 3$d$ orbitals equal to $U = 1.8$ eV and $J = 0.8$ eV, respectively. The interlayer exchange defined as $J_\perp = \Delta E/[6S^{(1)}S^{(2)}]$, with $S^{(1)}$ and $S^{(2)}$ being the layer-1 and layer-2 Ni-spins ($S = 1$) respectively, is $\simeq +3.1$ meV within the VASP calculations and $\simeq +2.8$ meV within the WIEN2k calculations. Similar results were also obtained by introducing the SOC and by using PBEsol[48] and optB86 (ref. [49]) exchange-correlation functionals, which proves the robustness of our results. A similar procedure applied to a NiBr₂ bilayer yields a much smaller interlayer AFM coupling of about $\simeq +1.2$ meV, indicating the extended I 5$p$ orbital states play a non-trivial role in mediating spin exchange across layers of NiI₂.

The $M$ tensor was evaluated following the no-substitution four-state method[38] performing DFT+U+SOC calculations with VASP on a $5 \times 4 \times 1$ supercell of the NiI₂ monolayer. We selected a pair of spins

# Article

($S_1$ and $S_2$) along the $x$ axis (parallel to the **a** lattice vector) and calculated the Berry-phase polarization arising from different sets of four non-collinear spin configurations, defining the $M$ tensor, in units of $10^{-5}$ e Å, as

$$M = \begin{bmatrix} (P_{12}^{yz})_x & (P_{12}^{zx})_x & (P_{12}^{xy})_x \\ (P_{12}^{yz})_y & (P_{12}^{zx})_y & (P_{12}^{xy})_y \\ (P_{12}^{yz})_z & (P_{12}^{zx})_z & (P_{12}^{xy})_z \end{bmatrix} = \begin{pmatrix} 20 & 0 & 32 \\ 0 & 348 & -520 \\ 0 & 25 & 0 \end{pmatrix} \quad (4)$$

The accuracy of the polarization values was checked by repeating calculations with a larger vacuum of about 32 Å and including dipole corrections.

## Data availability

The datasets generated during and/or analysed during the current study are available from the corresponding author on reasonable request.

41. Zomer, P., Guimarães, M., Brant, J., Tombros, N. & Van Wees, B. Fast pick up technique for high quality heterostructures of bilayer graphene and hexagonal boron nitride. *Appl. Phys. Lett.* **105**, 013101 (2014).
42. Kresse, G. & Furthmüller, J. Efficient iterative schemes for ab initio total-energy calculations using a plane-wave basis set. *Phys. Rev. B* **54**, 11169–11186 (1996).
43. Kresse, G. & Joubert, D. From ultrasoft pseudopotentials to the projector augmented-wave method. *Phys. Rev. B* **59**, 1758–1775 (1999).
44. Blaha, P. et al. WIEN2k: an APW+lo program for calculating the properties of solids. *J. Chem. Phys.* **152**, 074101 (2020).
45. Perdew, J. P., Burke, K. & Ernzerhof, M. Generalized gradient approximation made simple. *Phys. Rev. Lett.* **77**, 3865–3868 (1996).
46. Rohrbach, A., Hafner, J. & Kresse, G. Electronic correlation effects in transition-metal sulfides. *J. Phys. Condens. Matter* **15**, 979–996 (2003).
47. Liechtenstein, A. I., Anisimov, V. I. & Zaanen, J. Density-functional theory and strong interactions: Orbital ordering in Mott-Hubbard insulators. *Phys. Rev. B* **52**, R5467–R5470 (1995).
48. Perdew, J. P. et al. Restoring the density-gradient expansion for exchange in solids and surfaces. *Phys. Rev. Lett.* **100**, 136406 (2008).
49. Becke, A. D. On the large-gradient behavior of the density functional exchange energy. *J. Chem. Phys.* **85**, 7184–7187 (1986).

**a**



(0 0 3) (0 0 6) (0 0 9) (0 0 12) (0 0 15) (0 0 18)

X-ray Counts [arb.]

2θ [deg]

**b**



(0 0 3) (0 0 6) (1 0 4) (sample holder) (0 0 9) (1 0 -8) (0 0 12) (0 0 15) (1 0 16) (0 0 18)

X-ray Counts [arb.]

2θ [deg]

**c**



SiN$_x$

NiI$_2$

5um

**d**



**Extended Data Fig. 1 | X-ray and electron diffraction of NiI$_2$ crystals. a**, X-ray diffraction of a CVT-grown NiI$_2$ single crystal along the **c**-axis. **b**, X-ray powder diffraction of CVT-grown NiI$_2$. **c**, An optical image of a 7 nm PVD grown NiI$_2$ flake transferred onto a SiN$_x$ membrane. **d**, The electron diffraction pattern of the PVD grown NiI$_2$ flake shown in **c**, using a transmission electron microscope.
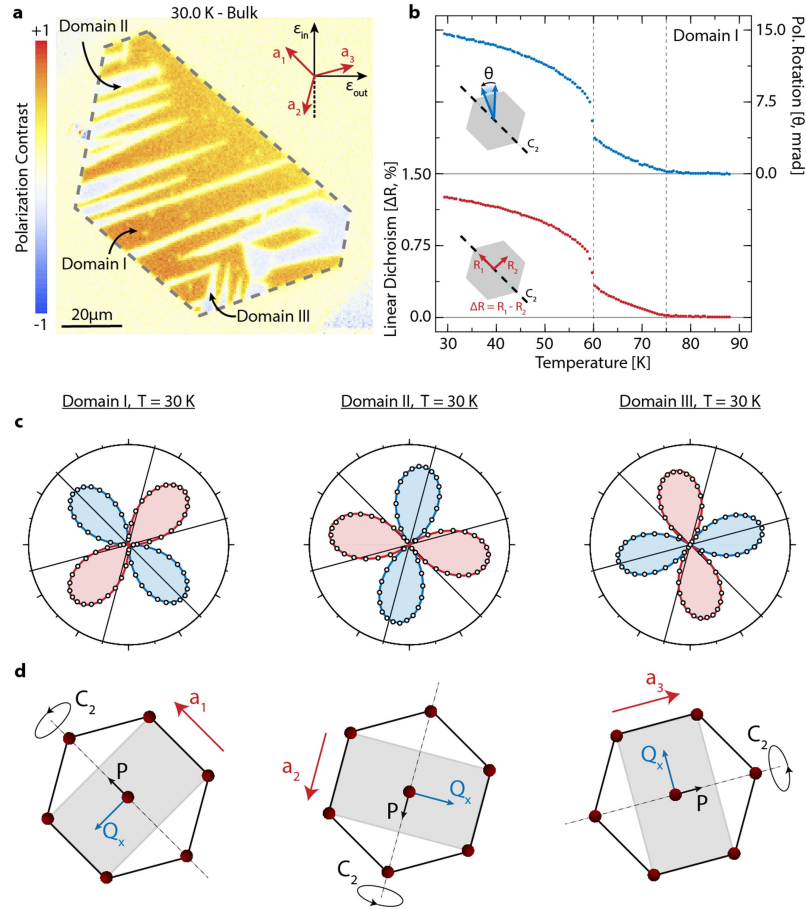
**Extended Data Fig. 2 | Linear dichroism and birefringence-induced polarization rotation measurements in bulk NiI$_2$. a**, Polarized microscopy image of bulk NiI2. The positions where the optical measurements were performed are labelled as Domain I-III. **b**, Comparison of the temperature-dependent birefringence-induced polarization rotation (top) and linear dichroism (bottom) on Domain I. **c**, Angular-dependent linear dichroism measurements from the three distinct domains identified in **a**. Radial lines indicate the crystallographic **a**-axes determined from the edges of the as-grown PVD sample. **d**, Schematics of the domains as identified from AD-LD measurements in **c**, denoting the local $C_2$ axis orientation, the polar vector **P** and the in-plane component of the helimagnetic ordering vector **Q**.
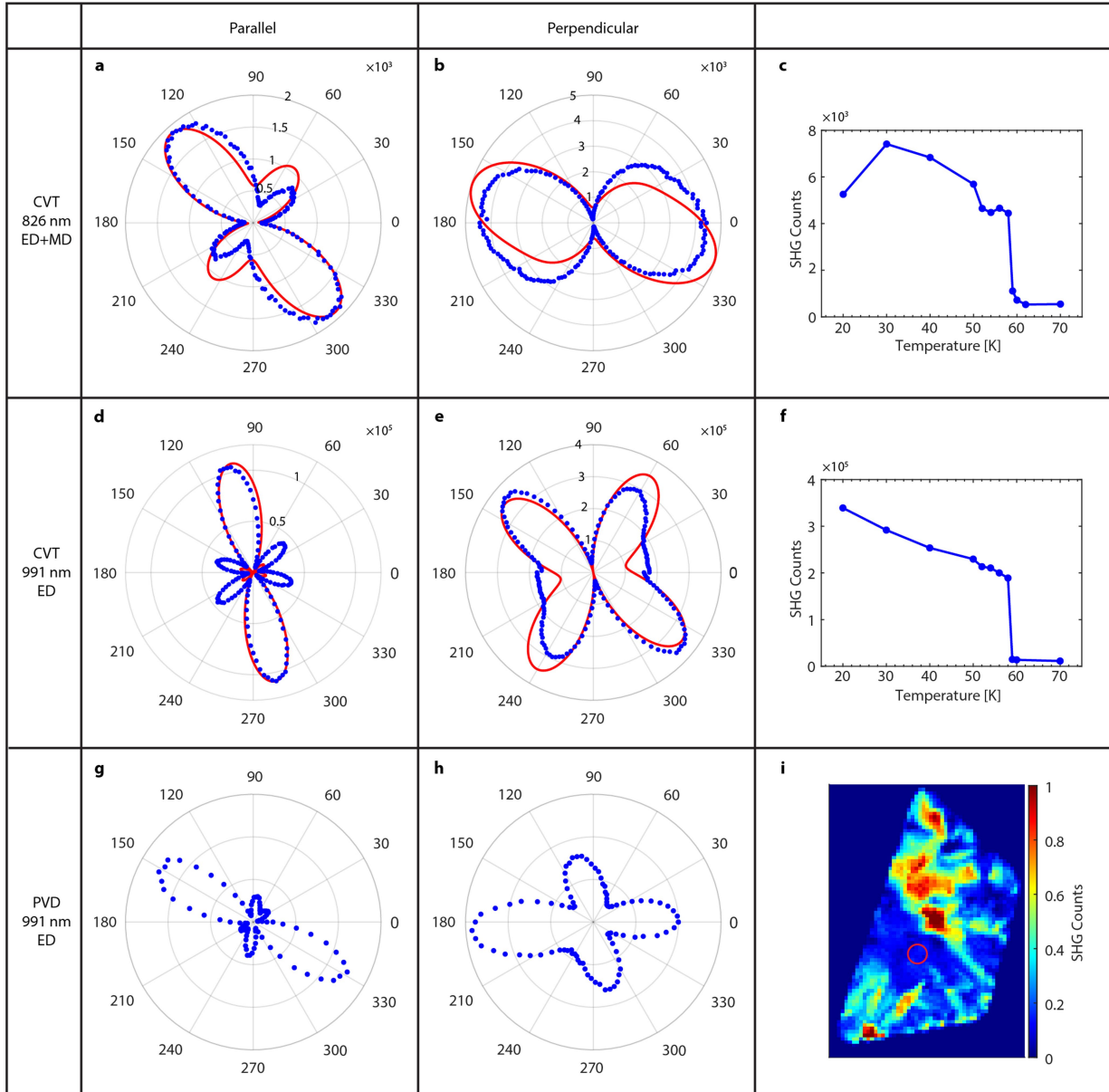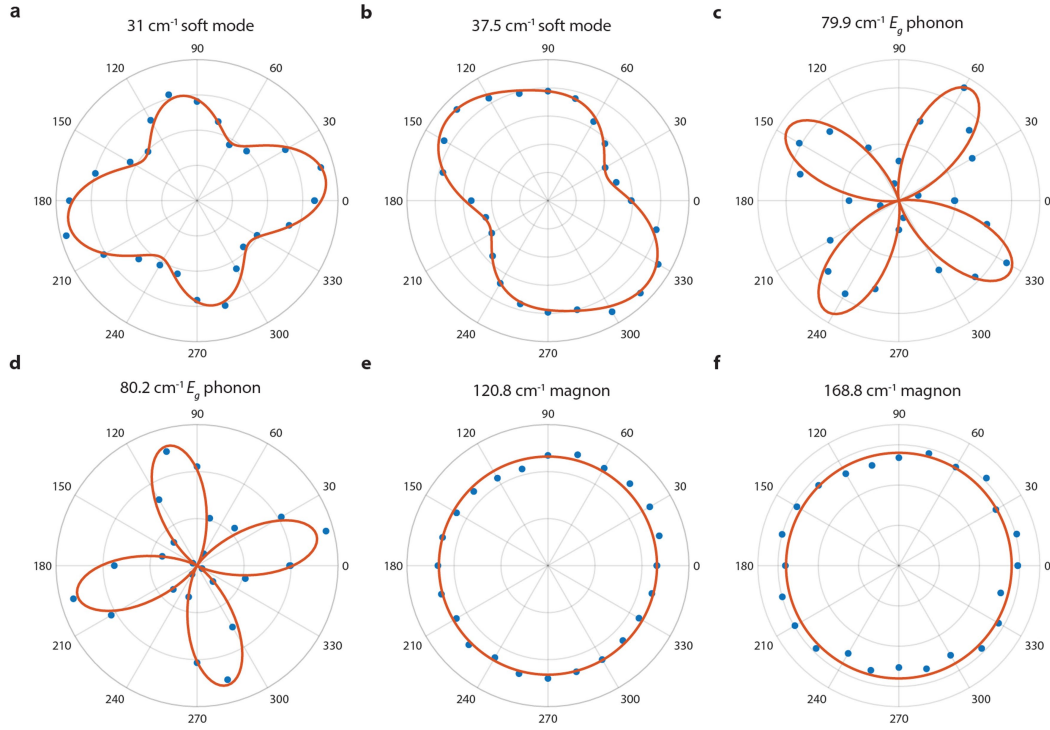
**Extended Data Fig. 3 | Wavelength-dependent Second Harmonic Generation of NiI₂.** Rotational anisotropy SHG (RA-SHG), fits to nonlinear tensor elements and their temperature dependence on a single domain CVT grown bulk NiI₂ using **a**–**c**, 826 nm laser, and **d**–**f**, 991 nm laser. The RA-SHG traces obtained with 826 nm can only be fit with a combination of electric dipole (ED) and magnetic dipole (MD) radiation, whereas the RA-SHG traces obtained with 991 nm only exhibit ED component. **g, h**, RA-SHG on PVD grown bulk NiI₂ samples shows the same signatures as the CVT grown samples. **i**, SHG imaging of the PVD sample at 15 K. The red circle shows the single domain region where the RA-SHG was taken.
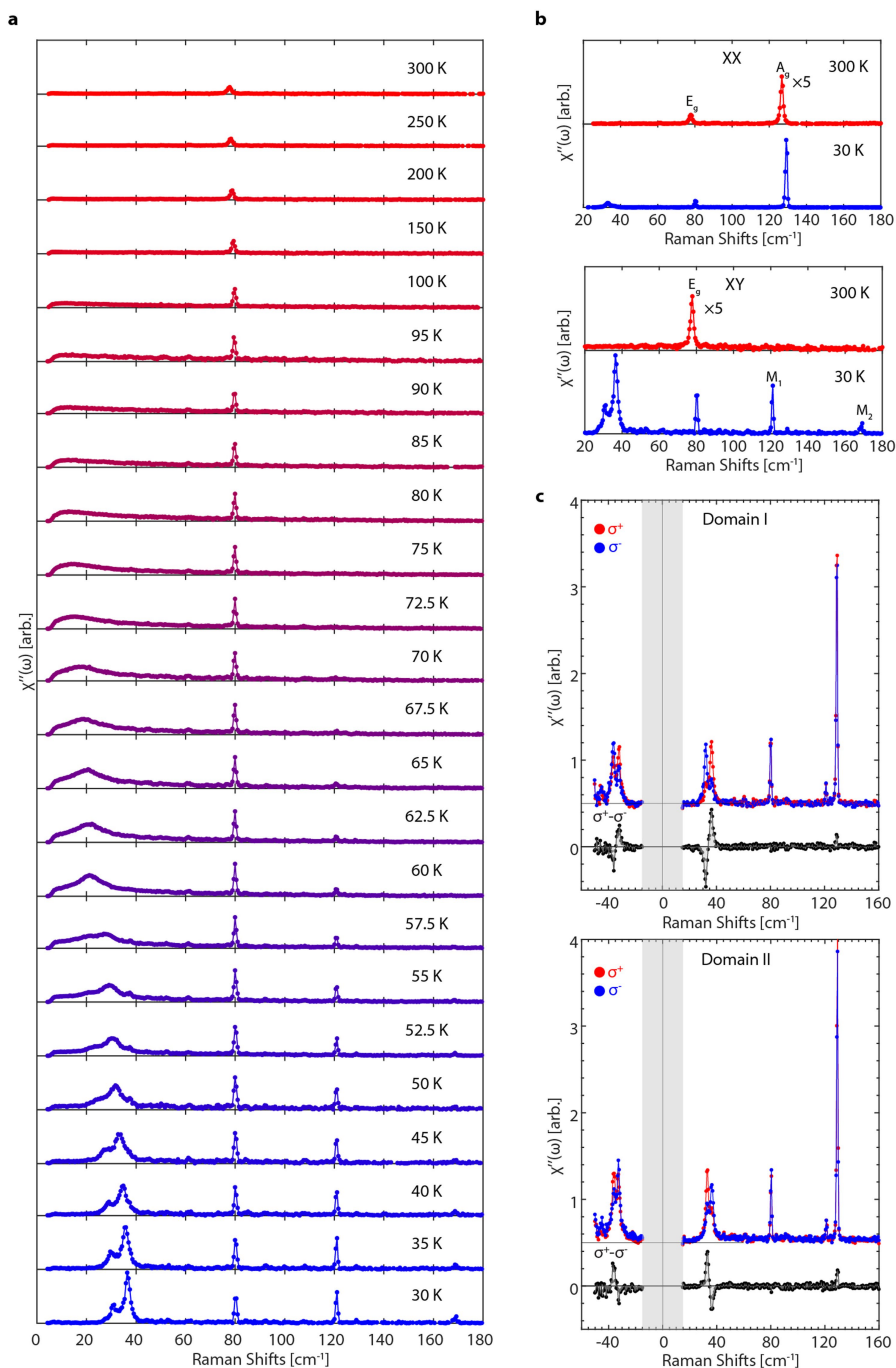
**Extended Data Fig. 4 | Temperature-dependent polarized Raman spectra of bulk NiI$_2$. a**, Raman data in the cross-polarized XY channel from 30 K to 300 K. **b**, Comparison of the cross-polarized (XY) and parallel-polarized (XX) channels at high and low temperature. **c**, Circularly polarized Raman spectra at 30 K on domain I and domain II regions for $\sigma^+/\sigma^-$ incident polarization (top) and the net ROA ($\sigma^+-\sigma^-$) (bottom).

**a** 31 cm⁻¹ soft mode

**b** 37.5 cm⁻¹ soft mode

**c** 79.9 cm⁻¹ $E_g$ phonon

**d** 80.2 cm⁻¹ $E_g$ phonon

**e** 120.8 cm⁻¹ magnon

**f** 168.8 cm⁻¹ magnon

**Extended Data Fig. 5 | Angular Resolved Polarized Raman Spectroscopy (ARPRS) in cross-polarized (XY) configuration. a, b,** The ARPRS polar plots of the 31 cm⁻¹ and 37 cm⁻¹ modes appearing in the multiferroic phase. Neither agrees with a pure phonon or magnon mode, suggesting they may be consistent with electromagnons. **c, d,** The 80 cm⁻¹ peak is composed of two phonons below $T_{N,2}$, one at 79.9 cm⁻¹ and the other at 80.2 cm⁻¹. These closely-spaced phonon modes display out-of-phase modulation with respect to the incident linear polarization and both display an $E_g$ symmetry with respect to the high-temperature $R\bar{3}m$ phase. **e, f,** The 120.8 cm⁻¹ and 168.8 cm⁻¹ are magnon modes. Red lines: ARPRS fits to the Raman tensors for different mode symmetries.
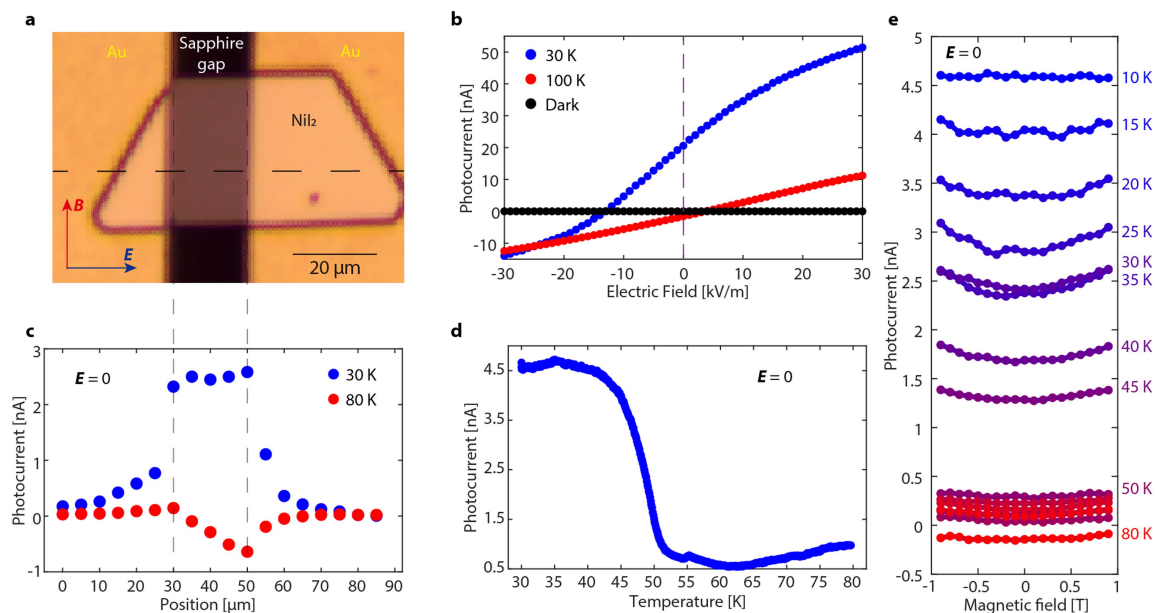
**Extended Data Fig. 6 | Bulk photovoltaic effect (BPE) in bulk NiI$_2$. a**, Optical image of the BPE device. A PVD grown bulk-like NiI$_2$ flake was transferred across a sapphire gap, bridging two gold pads as electrodes. The electric field was applied between the electrodes and in a direction nearly parallel to the $a$-axis, while the magnetic field was applied perpendicular to the electric field in plane. **b**, The electric field dependence of the photocurrent at 30 K, in the multiferroic phase and at 100 K, in the paramagnetic phase, reveals the presence of a polarization-induced internal electric field the multiferroic phase. **c**, The position dependence of the photocurrent along the dashed line in **a**, under zero bias shows a major contribution of the photocurrent from the NiI$_2$ between the electrodes. **d**, The temperature dependence of the zero-bias photocurrent shows a strong enhancement in the multiferroic phase. **e**, The external magnetic field increased the zero-bias photocurrent by 10–15%, which we ascribe to an increase of the electric polarization from magnetoelectric coupling. Linearly polarized 532 nm light (0.3 mW power) was used in the BPE measurement.
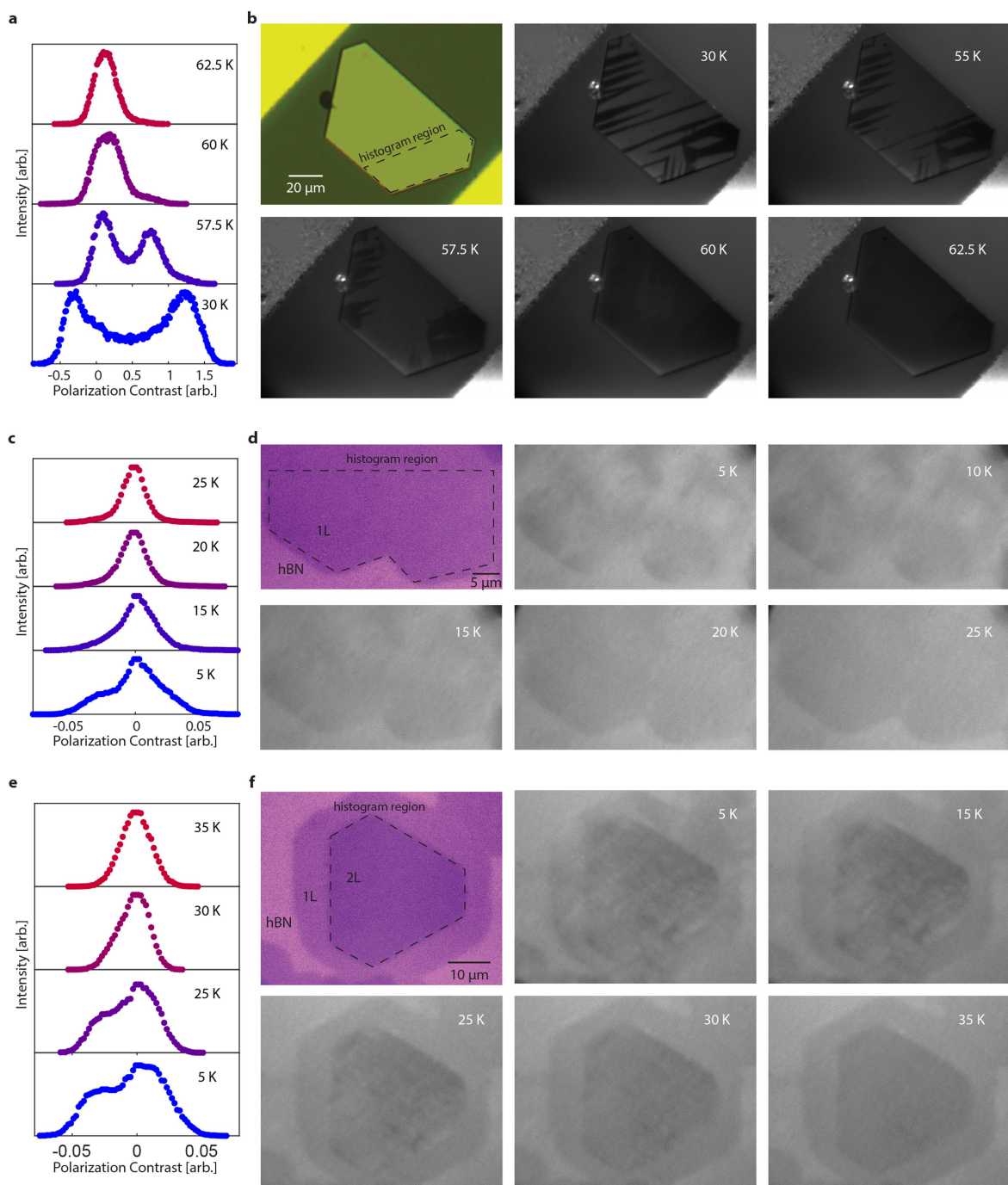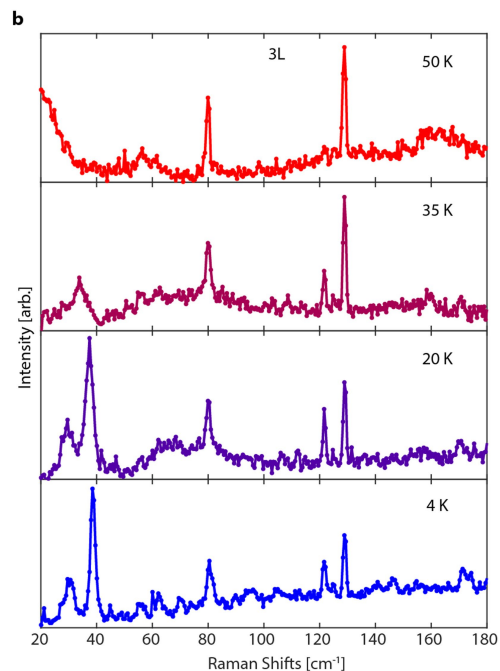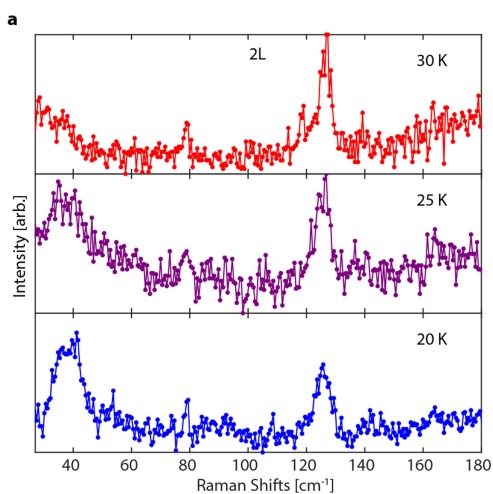
**Extended Data Fig. 7 | Cross-polarization images of the bulk, 1- and 2-layer NiI₂.** Temperature-dependent histogram plots of the polarization contrast images for **a**, bulk, **c**, 1-layer region and **e**, 2-layer region. The upper-left images in **b, d, f** show optical images of bulk, 1- and 2-layer NiI₂ flakes, respectively. Subsequent images depict the temperature-dependent polarization contrast images for key temperatures. The raw cross-polarization images at various temperatures across the multiferroic transition provide signatures of the domain dynamics, explaining the spatial inhomogeneity of the transition temperature identified through polarization rotation measurements. The domain texture vanishes in **d**, 1-layer near 20 K, and in **f**, 2-layer near 35 K, consistent with polarization rotation measurements (Fig. 2d).
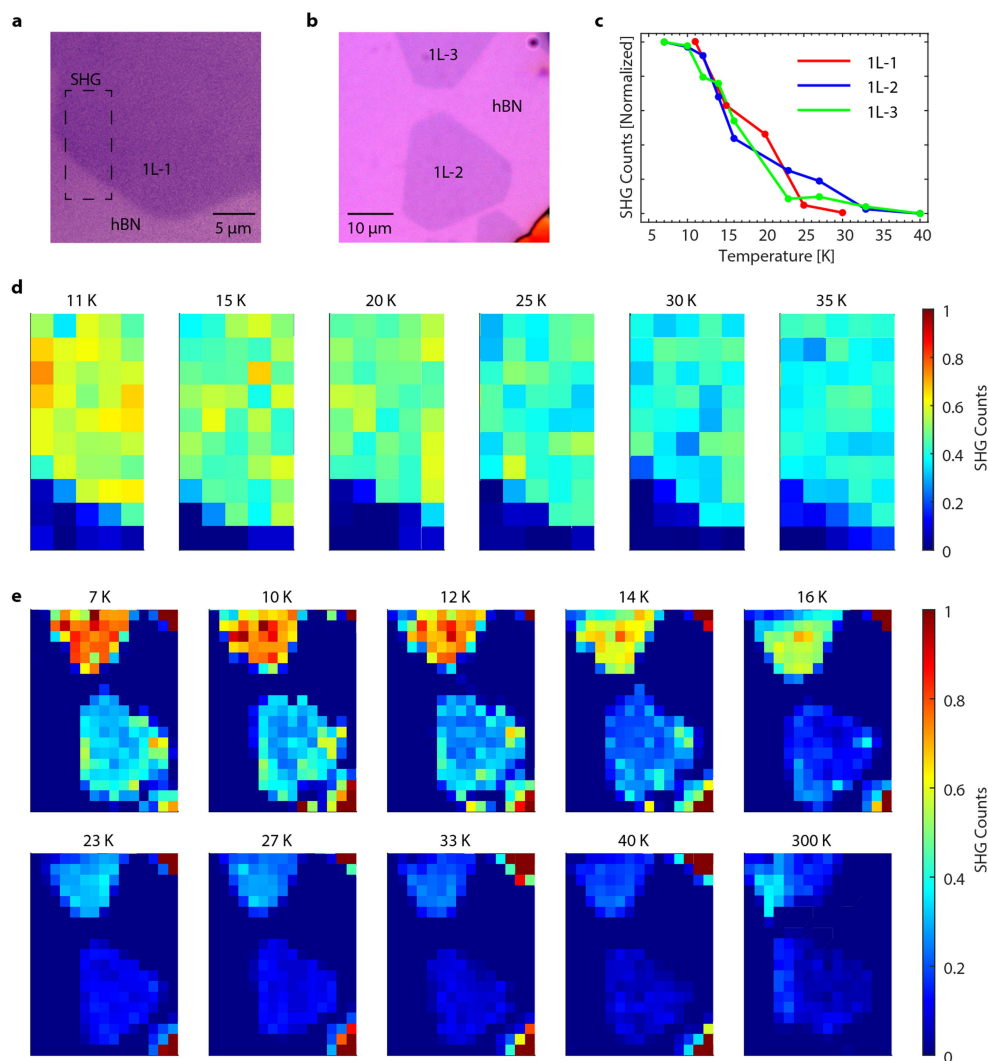
**Extended Data Fig. 8 | Temperature dependent Second Harmonic Generation imaging of the single-layer NiI$_2$ crystals. a, b,** Optical images of the region where the SHG imaging was performed. **c,** Integrated SHG counts on three single-layer NiI$_2$ crystals show a transition around 20 K, which is consistent with the polarization rotation measurement. **d,** Temperature dependent SHG imaging of the rectangular region in **a** using 780 nm excitation. **e,** Temperature dependent SHG imaging of the region in **b** using 991 nm laser. Colorbar: SHG counts.

**Extended Data Fig. 9 | Temperature dependent Raman Spectroscopy of two- and three-layer NiI$_2$ in cross-polarized (XY) configuration.** The soft modes at around 38 cm$^{-1}$ in **a**, 2-layer and **b**, 3-layer built up below 25 K and 35 K respectively, which are consistent with the transition temperature measured from polarization rotation and SHG.
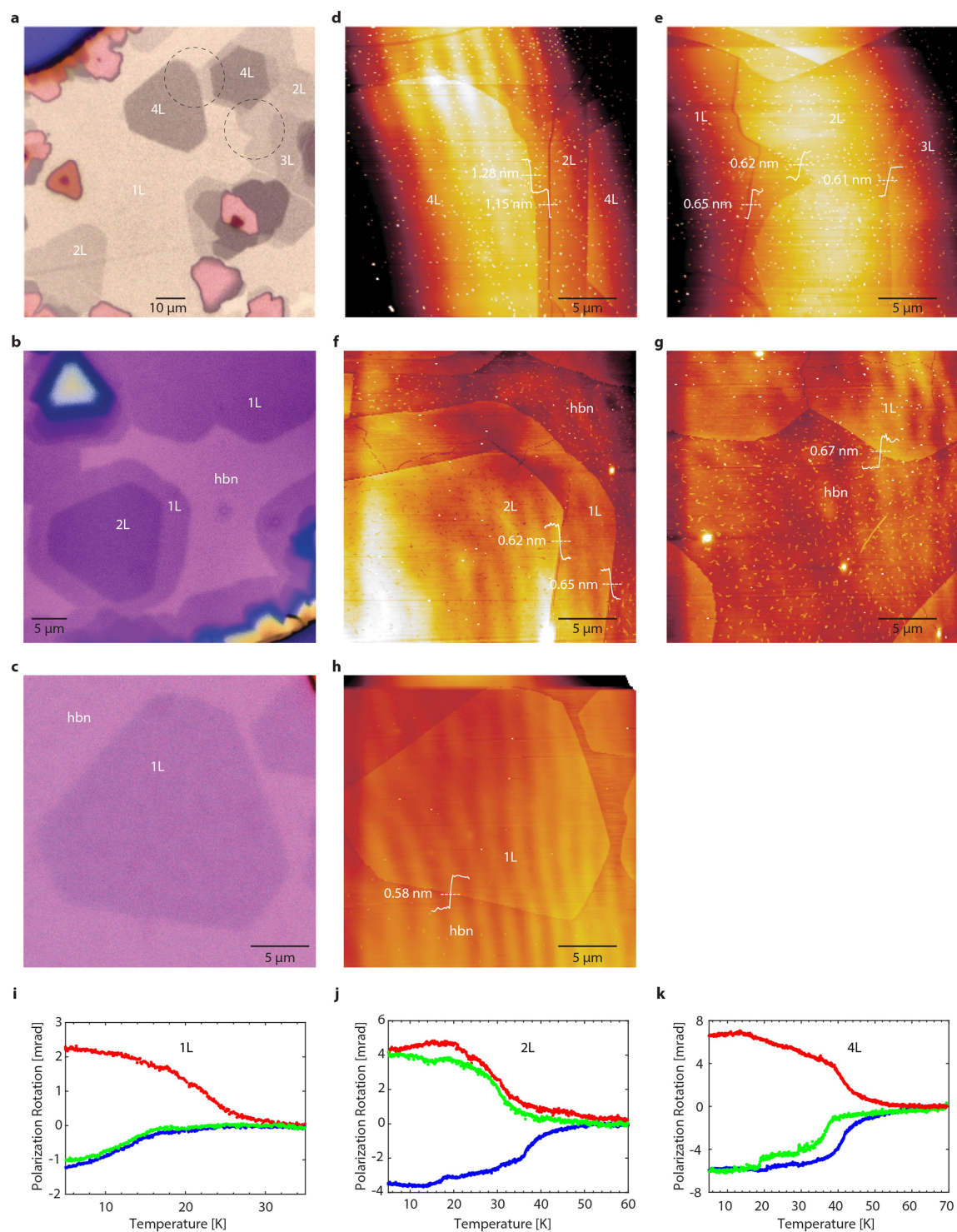
**Extended Data Fig. 10 | Atomic Force Microscopy and additional polarization rotation measurements on few-layer NiI$_2$ crystals.**
**a–c**, Wide-field optical images of one- to four-layer NiI$_2$ samples used in the optical measurements. **d–h**, Corresponding AFM maps of the region shown in the optical images. **i–k**, Temperature dependent polarization rotation measurements on one- to four-layer samples in different domain regions.